

# Experimental quantum verification in the presence of temporally correlated noise

S. Mavadia,<sup>1,2,\*</sup> C. L. Edmunds,<sup>1,2,\*</sup> C. Hempel,<sup>1,2</sup> H. Ball,<sup>1</sup> F. Roy,<sup>1</sup> T. M. Stace,<sup>3</sup> and M. J. Biercuk<sup>1,2</sup>

<sup>1</sup>*ARC Centre for Engineered Quantum Systems, School of Physics, The University of Sydney, NSW Australia*

<sup>2</sup>*National Measurement Institute, West Lindfield NSW 2070 Australia*

<sup>3</sup>*ARC Centre for Engineered Quantum Systems, School of Physics and Mathematics, The University of Queensland, St Lucia, QLD Australia*

(Dated: Tuesday 21<sup>st</sup> June, 2022 at 00:56)

Growth in the complexity and capabilities of quantum information hardware mandates access to practical techniques for performance verification which function under realistic laboratory conditions. Here we experimentally characterise the impact of common temporally correlated noise processes on both randomised benchmarking (RB) and gate-set tomography (GST). We study these protocols using an analytic toolkit based on a formalism mapping noise to errors for arbitrary sequences of unitary operations. This analysis highlights the role of sequence structure in enhancing or suppressing the sensitivity of quantum verification protocols to temporally correlated noise. We perform experiments with a single trapped  $^{171}\text{Yb}^+$  ion as a qubit and inject engineered detuning noise ( $\propto \hat{\sigma}_z$ ) with different temporal correlations in order to quantitatively probe protocol performance. Experiments on RB validate predictions that the distribution of measured fidelities over sequences is described by a gamma distribution varying between approximately Gaussian for uncorrelated noise and a broad, highly skewed distribution for temporally correlated noise; we find agreement with first-principles calculations of the relevant shape and scale parameters in both regimes. For GST, we use both the protocol's in-built numeric toolkit and experiments with engineered detuning errors to demonstrate that GST underestimates reported diamond norms of both driven operations when subject to strongly correlated  $\hat{\sigma}_z$  noise.

Quantum characterisation, validation, and verification (QCVV) techniques are broadly used in the quantum information community in order to characterise the performance of experimental hardware. A variety of techniques have emerged including randomised benchmarking (RB) [1, 2], purity benchmarking [3], process tomography [4–7], adaptive methods [8], and gate-set tomography (GST) [9, 10]. Each protocol has relative strengths and weaknesses; for instance, RB has low experimental overhead but only provides average information about gate performance, while process tomography provides more information at the cost of unfavourable scaling in measurement overhead [11]. Despite their differences, these protocols share the common theme that they were originally developed and mathematically formalised assuming that error processes are uncorrelated in time.

Even in highly controlled laboratory environments there are a range of noise sources which, when applied to a qubit concurrent with logical gate operations, produce effective error models that diverge significantly from the assumptions underlying most QCVV protocols. For example, slow variations in ambient magnetic fields or drifts in amplifier gain can produce noise processes that exhibit strong temporal correlations, often characterised through a power spectral density possessing large weight at low frequencies [12–14]. So far such processes have been largely ignored in experimental QCVV, with predominantly phenomenological attempts used to explain deviations from ideal outputs [15]. Understanding that such an approach is untenable when attempting to rigorously compare QCVV results to metrics relevant to quantum error correction has recently led to an expansion of theoretical activity in this space [16–20].

In this work our objectives are to experimentally characterise and explain the impact of temporally correlated noise processes on the outputs of QCVV protocols, and to identify potential modifications enabling users to improve the utility of the information returned. We perform comparative QCVV experiments using a single trapped  $^{171}\text{Yb}^+$  ion as a long-lived, high-stability qubit. Our study implements engineered frequency noise in the control system with user-tunable temporal correlations in order to controllably study the impact of these parameters on QCVV results. Measurements reveal that in the presence of noise with strong temporal correlations QCVV outputs can diverge significantly from expected “mean” behavior, highlighting potential circumstances where the information extracted from a given protocol may no longer accurately represent the true error processes experienced by individual gates. Our experiments are compared against analytic calculations linking the underlying structure of the QCVV protocols with the manifestation of specific signatures of noise correlations.

We examine two common QCVV protocols in the experimental quantum information community: RB and GST. The construction of these protocols follows a similar pattern, a series of unitary quantum operations is applied to one or more qubits sequentially in time, followed by a projective measurement (Fig. 1a). With fixed system parameters and for a given unitary sequence implementing a known net operation, the protocol may be repeated a number of times to sample the noise process, followed by an ensemble average over noise realisations to estimate the fidelity. Experimental parameters are changed according to some prescription (e.g. changing the sequence length,  $J$ ) and further data are collected. The variation in QCVV protocols comes through the process by which the constituent operations are chosen and the analysis techniques by which measurement results are post-processed to extract useful information.

\* These two authors contributed equally to this work.

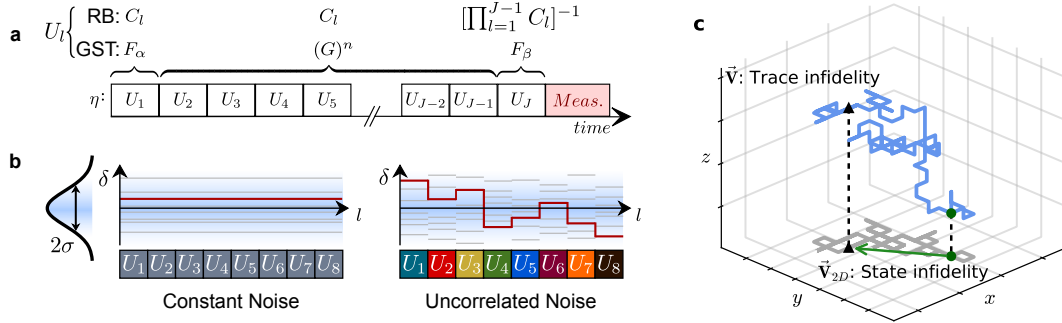


FIG. 1. QCVV sequence construction and mapping to accumulated error. **a** Overview of unitary sequence construction for RB and GST, using Clifford gates,  $C_l$  or fiducial operations,  $F_{\alpha,\beta}$  and repeated germs  $(G)^n$  respectively. **b** Schematic representation of constant and uncorrelated noise with relevant time scales defined by the sequence where  $\delta$  represents the instantaneous noise values drawn from a normal distribution with  $\sigma^2$  variance. Grey lines are other possible noise realisations. **c** Sequence-dependent “random walk” calculated for an arbitrary QCVV sequence (here according to the RB prescription) with  $J = 100$  in Pauli space. Green dot indicates origin and black triangle indicates sequence terminus. Blue line represents the 3D walk which can be used to calculate the trace infidelity while grey represents the 2D projection which is equivalent to the state infidelity, and is measurable in a standard projective measurement. Green arrow indicates the net walk vector,  $\vec{V}_{2D}$ , given unit step size.

In RB, sequences are constructed by concatenating unitary operations  $U_l$  selected at random from the 24 Clifford operations  $C_l$ . The final operation in a sequence of length  $J$  is selected to invert the net rotation  $U_J = (\prod_{l=1}^{J-1} C_l)^{-1}$ , such that the sequence implements a net identity  $\prod_{l=1}^J C_l = \hat{\mathbb{I}}$ . In GST, by contrast, operations are selected deterministically according to a tabulated routine comprising specifically crafted sequences that are designed to maximise sensitivity to particular error types. These operations are constructed by concatenating so-called “germs”, short sequences implementing predefined unitary rotations, which themselves are constructed from a subset of Clifford gates. The first and last unitaries  $U_{1,J} \in \{F_\alpha, F_\beta\}$ , termed the “fiducial” operations, effectively set the reference frame for state-preparation and measurement (Fig. 1a), see methods for more detail.

We compare the outputs obtained from both RB and GST for two distinct noise-correlation regimes. Firstly where the engineered noise is constant-valued over the entire sequence, representative of low frequency noise that introduces strong, temporally correlated, errors or secondly where the noise is high frequency which leads to uncorrelated errors between gates. We denote these two noise regimes as “constant” and “uncorrelated” respectively (Fig. 1b). Each sequence is exposed to  $N$  different noise realisations in order to average over an appropriate ensemble. We now introduce a shared framework for interpreting the impact of sequence structure and noise correlations on measurement outcomes in an effort to facilitate a comparative analysis of our experimental results.

## I. Results

### A. Mapping noise to measured error in QCVV

The key analytic tool for our study is a formalism mapping an applied noise model to an output error for a given QCVV sequence, following a procedure derived in [18]. Error accumulation over a given Clifford sequence maps to a “random walk” in a three-dimensional vector-space representing the ac-

tion of sequential error unitaries in the operator space spanned by the Pauli operators,  $\hat{\sigma}_{\{x,y,z\}}$  (Fig. 1c). For  $\hat{\sigma}_z$  noise, the  $l^{\text{th}}$  step of the walk is calculated by conjugating  $\hat{\sigma}_z$  with the entire operator subsequence  $K_{l-1} \equiv \prod_{q=1}^l U_q$  up to the  $l^{\text{th}}$  gate. This conjugation always results in a member of the Pauli group, allowing us to compactly write  $\mathbf{P}_l \equiv K_{l-1} \hat{\sigma}_z K_{l-1}^\dagger = \hat{r}_l \cdot \vec{\sigma}$ , where  $\vec{\sigma} = (\hat{\sigma}_x, \hat{\sigma}_y, \hat{\sigma}_z)$  and  $\hat{r}_l \in \{\pm \hat{x}, \pm \hat{y}, \pm \hat{z}\}$ . The direction of  $\mathbf{P}_l$  in Pauli space therefore maps to the Cartesian unit vector  $\hat{r}_l$  associated with the  $l^{\text{th}}$  step of a  $J$ -step walk  $\vec{R} \equiv \sum_{l=1}^J \delta_l \hat{r}_l$ . The step length,  $\delta_l$ , captures the integrated phase between the driving field and qubit during execution of the single gate  $U_l$ . In terms of experimental parameters,  $\delta_l = |\theta| \Delta / 2\Omega$ , where  $|\theta|$  is a measure of the evolution time of the applied unitary and  $\Delta / \Omega$  is the detuning (see *Methods*).

The overall form of the walk is a statistical measure of how the sequence itself interacts with the noise process to produce a net, measurable accumulation of error. Sequences that are highly susceptible to error accumulation produce walks that migrate far from the origin, while sequences exhibiting error suppression produce walks that meander back towards the origin. The net walk length is captured in the mean-squared distance from the origin  $\langle \|\vec{R}\|^2 \rangle$ , averaged over noise realisations. This links to the “trace fidelity”, defined as  $\mathcal{F}_{\text{trace}} = \langle |\text{Tr}(\prod_{l=1}^J \tilde{U}_l)|^2 \rangle / 4$ , where  $\tilde{U}$  are modified unitary operations to take into account the effect of the  $\hat{\sigma}_z$  noise. We then define the infidelity  $\mathcal{I}_{\text{trace}} = 1 - \mathcal{F}_{\text{trace}} \simeq \langle \|\vec{R}\|^2 \rangle$ .

Appropriately linking this picture of error accumulation to standard laboratory measurements requires consideration of the measurement routine itself. In typical measurements the qubit Bloch vector at the end of the sequence is projected onto the quantisation axis,  $z$ , with basis states  $|0\rangle$  and  $|1\rangle$ . A measurement of this type is therefore insensitive to net rotations around that axis of the Bloch sphere, meaning that it only probes a 2D projection of the 3D walk onto the  $xy$ -plane. Our preferred metric is the state fidelity which may be linked di-

rectly to such a 2D projection (grey line, Fig. 1c) as  $\mathcal{I}_{\text{state}} = 1 - \mathcal{F}_{\text{state}} = \langle \|\vec{R}_{2D}\|^2 \rangle$  where  $\mathcal{F}_{\text{state}} = \langle \|\langle 0 | \prod_{l=1}^J U_l | 0 \rangle\|^2 \rangle$ ,  $\langle \|\vec{R}_{2D}\|^2 \rangle = \langle \|\vec{R}\|^2 \rangle - \langle \|\vec{R}_z\|^2 \rangle$ , and  $\langle \|\vec{R}_z\|^2 \rangle$  is the mean-squared walk length along the quantisation axis (see *Supplementary Material* for details). From here we implicitly refer to all measured fidelities as state fidelities and henceforth drop the subscripts for  $\mathcal{F}$  and  $\mathcal{I}$ .

At this stage we must link the correlation properties of the noise to the form of the walk for a specific sequence. Considering only the underlying properties of the sequence, we may assume unit-length steps, resulting in a deterministic sequence-dependent walk with normalised length  $\vec{V} \equiv \sum_{l=1}^J \hat{r}_l$ . The presence or absence of temporal noise correlations is now captured through a rescaling of the individual steps in the deterministic walk for a specific sequence. In the case of constant noise, the net error can be separated into two independent parts,  $\|\vec{R}\|^2 = \delta^2 \|\vec{V}\|^2$ , where  $\delta$  is the amplitude of the noise and  $\|\vec{V}\|$  is the net unit-step walk specific to a particular sequence. However, in the case of uncorrelated noise these two terms are no longer separable and the net error must be calculated as the product of the noise amplitude and each individual step in the random walk,  $\|\vec{R}\|^2 = \|\sum_{l=1}^J \delta_l \hat{r}_l\|^2$ .

### B. Experimental platform and engineered noise

We perform experiments using the hyperfine qubit in a single trapped  $^{171}\text{Yb}^+$  ion driven by microwaves near 12.64 GHz. Our calibration process permits accurate determination of the (first-order magnetic-field-insensitive) qubit transition frequency to within approximately 1 Hz. In our laboratory, this qubit and the associated control system have been demonstrated to possess a coherence time of  $T_2 \sim 1$  s, measurement fidelity of  $\sim 99.7\%$ , and error rates from intrinsic system noise of  $p_{RB} \approx 6 \times 10^{-5}$  using “baseline” RB experiments (see supplementary figures). Details of the control system, measurement procedure, and experimental protocols for QCVV techniques used here are presented in the methods.

We engineer  $\hat{\sigma}_z$  noise applied concurrently with Clifford operations through the application of a detuning,  $\Delta(t)$ , of the qubit driving field from resonance using an externally modulated vector signal generator. As the detuning is applied concurrently with driven qubit rotations about  $x$  and  $y$  axes, rotation errors arise along multiple directions on the Bloch sphere, rather than being purely  $\hat{\sigma}_z$  in character. An additional violation of typical assumptions employed in QCVV is that different Clifford gates are physically decomposed into base rotations with different durations which means that our formal error model will also be gate-dependent [21]. In our experiments we vary between the two noise cases, constant and uncorrelated, but set the distribution of noise  $\Delta(t)/\Omega \sim \mathcal{N}(0, \sigma^2)$ , where  $\sigma^2$  is the variance of the distribution, such that the root-mean-square value is approximately equivalent in both cases once averaged over all noise realisations, see supplementary information for more details on the error model.

Experiments involve state preparation in the  $|0\rangle \equiv |^2\text{S}_{1/2} |F=0, m_F=0\rangle$  state, application of a unitary sequence appropriate for a QCVV protocol while subject to noise, and projective measurement of the qubit along the

quantisation axis. The sequence of operations applied and the measurement procedure are determined by the protocol in use.

### C. RB fidelity distributions

Measurement outcomes for different RB sequences are characterised by distributions with distinctly different shapes depending on the temporal correlations in the noise. By taking advantage of this information we are able to learn about the nature of the particular error process. However, the standard practice of combining all measurements to extract an RB error rate results in a global ensemble average, ignoring this

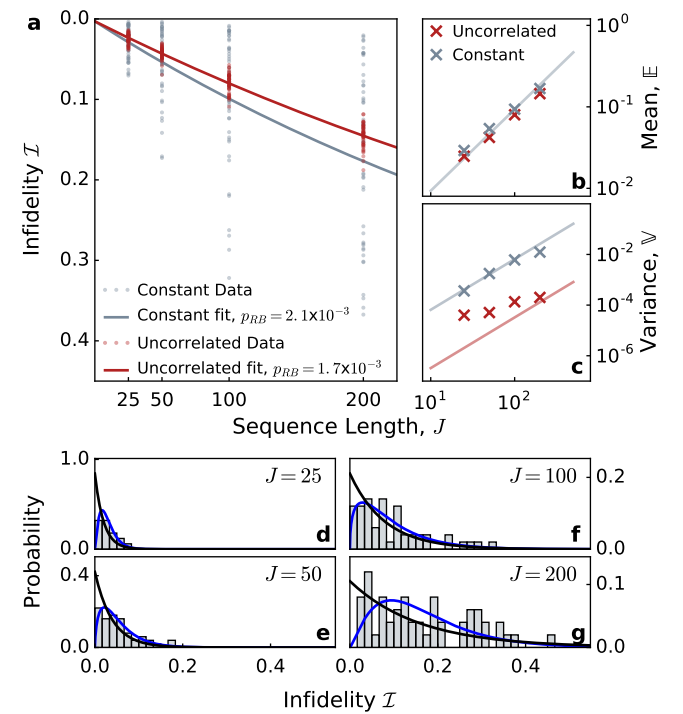


FIG. 2. RB distributions over sequences in the presence of different noise correlations. **a** Standard RB protocol showing fidelity as a function of  $J$  for the same set of sequences implemented under constant (grey) or uncorrelated (red) noise with  $\Delta_{\text{RMS}} = 1$  kHz. In these experiments the Rabi frequency,  $\Omega = 22.5$  kHz. Each experiment is repeated  $r = 25$  to  $r = 30$  times under fixed conditions, and each sequence fidelity is averaged over 200 noise realisations. Lines represent exponential fits to the sequence-averaged infidelity  $\bar{I} = 1 - \mathcal{F}(J) = 0.5 - (0.5 - \rho)e^{-p_{RB}J}$ , weighted by the variance over sequences for each  $J$ , and are used to extract  $p_{RB}$ . Here  $\rho = 3 \times 10^{-3}$  represents state preparation and measurement error. **b-c** Scaling of  $\mathbb{E}(\mathcal{I})$  and  $\mathbb{V}(\mathcal{I})$  against sequence length  $J$ , comparing experimental values (markers) against first-principles theory (lines) as per [18] modified to state fidelity (2D walk) and noise applied concurrently with gate implementation. See Methods for details. **d-g** Histograms for data in panel **a** in the presence of constant noise. Blue line: calculated gamma distribution taking as input shape and scale parameters extracted from measured distribution. Black line: gamma distribution using input parameters calculated from first principles (see text).

effect. We implement a set of randomly compiled Clifford sequences, fidelities for each sequence of length  $J$  are averaged together and the decay of the sequence-averaged fidelity as a function of  $J$  is used to determine a single metric,  $p_{RB}$ . In the limit of uncorrelated noise, all such randomly selected sequences of length  $J$  are equivalent under noise averaging, and all sequence fidelities tend towards the mean. Recent theoretical studies have demonstrated that the presence of temporal noise correlations, by contrast, can result in a strong divergence between average and worst-case reported fidelities over different sequences with fixed length [18, 22].

In our experimental study we measure the noise-averaged fidelity distributions of a set of sequences  $\{\eta_i\}_J$ , indexed by  $i$  and of length  $J$ , for different lengths  $25 \leq J \leq 200$  (Fig. 2a), where we implement the same set of  $J$ -gate sequences under application of either uncorrelated or constant detuning noise. For an arbitrary individual sequence,  $\eta_i$  and a single noise realisation,  $n$ , possessing user-defined correlation properties, we perform  $r$  nominally identical repetitions of the experiment and average these together to produce a maximum-likelihood estimate of fidelity,  $\mathcal{F}_{i,n}$ . The use of multiple repetitions under identical conditions suppresses quantum projection noise in the qubit measurement. In general, we average measured fidelities over a fixed number of noise realisations to yield  $\mathcal{F}_{i,\langle \cdot \rangle}$  for a fixed sequence  $\eta_i$ . From here on, we will refer to this noise-averaged fidelity as  $\mathcal{F}$ .

In the case of uncorrelated noise we observe the distribution of sequence outcomes symmetrically spread around the sequence-averaged mean fidelity,  $\bar{\mathcal{F}}(J)$ , and the entire distribution shifts away from unit fidelity with increasing  $J$  (Fig 2a). The presence of constant noise, by contrast, produces a broad distribution of measured  $\mathcal{F}$  over each set  $\{\eta_i\}_J$ , demonstrating a positively skewed set of outcomes and the persistence of a long tail at higher error rates. In this case, as  $J$  increases the distribution broadens but remains skewed towards fidelities larger than  $\bar{\mathcal{F}}(J)$ . Under both noise correlation cases, the measured  $\bar{\mathcal{F}}(J)$  remain approximately the same. The differences in the distribution of measured fidelities over sequences under these two noise models reproduces the central predictions of Ref. [18].

Quantitative information may be extracted by comparing the characteristics of the distributions themselves against numerical predictions appearing in Ref. [18] for both constant and uncorrelated noise, beginning with the measured expectation,  $\mathbb{E}(\mathcal{I})$ , and variance,  $\mathbb{V}(\mathcal{I})$  (Fig. 2b-c). More specifically, theoretical predictions suggest that the distribution of outcomes under both noise models, and models that interpolate between these limits, will be well described by a gamma distribution [18]. The general gamma distribution probability density function is given by

$$f(x) = \frac{x^{\alpha-1}}{\Gamma(\alpha)\beta^\alpha} \exp\left[-\frac{x}{\beta}\right], \quad (1)$$

where  $\alpha$  and  $\beta$  are the shape and scale parameters and  $\Gamma(x)$  is the gamma function. The form of the gamma distribution will vary significantly between the limiting noise cases treated

here, tending towards a symmetric Gaussian for uncorrelated noise and a broader distribution skewed towards high fidelities in the presence of constant noise, as determined by the values of  $\alpha$  and  $\beta$ .

Figures 2d-g show histograms of fidelity outcomes over RB sequences in the presence of constant noise. We overlay a gamma distribution calculated from first principles using no free parameters (black lines), or by using the measured  $\mathbb{E}(\mathcal{I})$  and  $\mathbb{V}(\mathcal{I})$  of the data to calculate the shape and scale parameters of the gamma distribution (blue line) as  $\alpha = \mathbb{E}^2/\mathbb{V}$  and  $\beta = \mathbb{V}/\mathbb{E}$ . The measurement data agrees well with the gamma distribution obtained in the latter case across the full range of  $J$  and  $\mathcal{F}$ . We believe that divergence from first-principles calculations may be due to the presence of state-preparation and measurement errors in our experiments which distort the distribution near the highest fidelities, or contributions from higher-order analytic error terms. For details on modifications to the theory presented in [18] accounting for the specific noise and gate-dependent error model employed in our experiments see *Supplementary Material*.

#### D. Modification of RB for identification of model violation

The emergence of strongly sequence-dependent fidelities in the presence of constant noise is captured through simple examination of the walks for different sequences. Under correlated noise, certain sequences possess walks with large  $\|\vec{V}_{2D}\|^2$ , hence amplifying the accumulation of error, while others tend back towards the origin and show reduced accumulated error (Fig. 3a-b). We arbitrarily classify sequences as “long-walk” if they possess a 2D projection beyond the diffusive mean-squared limit for an unbiased random walk,  $\|\vec{V}_{2D}\|^2 > \frac{2}{3}J$ .

We link between the sequence walk in Pauli space and the noise-averaged fidelity by displaying the experimentally measured  $\mathcal{I}$  for sequences of fixed length  $J$  against the calculated 2D walk length,  $\|\vec{V}_{2D}\|^2$  (Fig. 3c). Data are presented for both uncorrelated (red open markers) and constant (grey solid markers) noise, where the same set of sequences is used between the noise models. Fidelity measurements for uncorrelated noise are fit with a line possessing slope approximately consistent with zero, while for the same sequences under constant noise, the measurements show a positive dependence on  $\|\vec{V}_{2D}\|^2$  as expected. We believe the significant scatter in the plot is likely due to a concurrently applied noise source and higher-order contributions to error, neither of which are incorporated in the first principles calculation of the walk,  $\|\vec{V}_{2D}\|^2$  (see appendix C of [18]). Nonetheless, the effect of sequence structure on measured fidelity is clearly visible for the case of constant noise.

In aggregate this phenomenology gives rise to the skewed and broadened gamma distribution described above under constant noise, and the convergence of all noise averaged fidelities for individual sequences to the ensemble average when the noise is temporally uncorrelated. However, pre-selection of RB sequences possessing large calculated walks also provides a mechanism to both identify the presence of temporally correlated noise and extract a RB outcome which more closely approximates worst-case errors. In Fig. 3d we

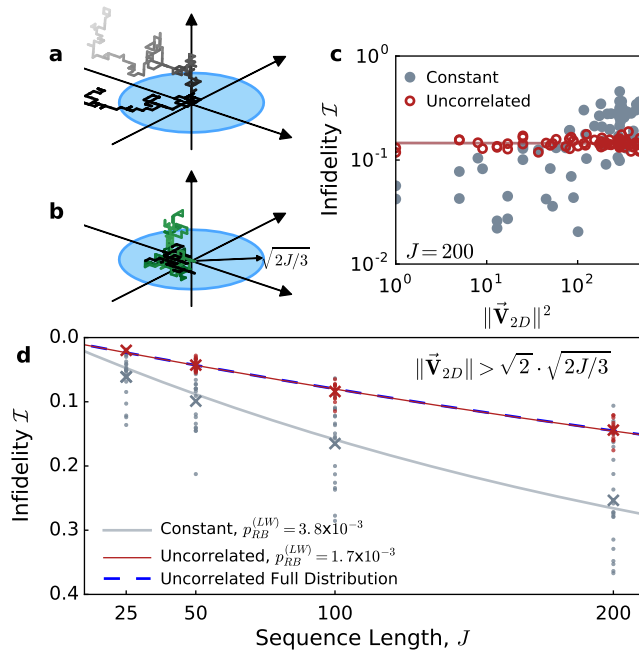


FIG. 3. RB using long-walk sequences. **a-b**) Schematic representations of long (a) and short (b) length walks under constant noise in 3D (coloured lines) and 2D (black lines), defined relative to a limit deduced from diffusive behaviour, as indicated by the blue circle. **c**) Noise-averaged fidelity distributions of the same sequences as a function of walk length in the 2D plane. Measured infidelity vs. 2D walk length,  $\|\vec{V}_{2D}\|^2$ , when subject to constant (grey) and uncorrelated noise (red) with linear fit overlaid. **d**) RB using long-walk sequences. Solid red line corresponds to RB performed using 20 long-walk sequences and uncorrelated noise. Extracted  $p_{RB}$  matches that extracted under the same conditions using an unbiased sampling of all sequences (dashed line). Grey line corresponds to RB using the same long-walk sequences and constant noise. For the exponential fits, state-preparation and measurement error,  $\rho$ , is fixed to  $3 \times 10^{-3}$ .

plot measured fidelity vs.  $J$  for a subset of sequences pre-selected to possess long walks as in Fig 3a-b, which we denote  $\mathcal{F}_{LW}(J)$ . Preselection of long walks is based on the condition  $\|\vec{V}_{2D}\|^2 > 2 \times \frac{2}{3}J$ .

When these long-walk sequences are subjected to uncorrelated noise, the distribution of fidelities over sequences remains approximately Gaussian-distributed about the mean, and the mean over this subset closely approximates the mean over an unbiased random sampling of the  $24^J$  possible  $J$ -gate sequences,  $\mathcal{F}_{LW}^{\text{uncorr.}} \approx \mathcal{F}^{\text{uncorr.}}$ , (Fig 2d, dashed line). However, in the presence of constant noise we observe a larger error rate than that achieved with unbiased sampling  $\mathcal{F}_{LW}^{\text{const.}} > \mathcal{F}^{\text{const.}}$ . The difference between the sequence-averaged mean fidelities in these noise cases arises solely because of the intrinsic properties of the sequences in use.

When plotting  $\mathcal{F}_{LW}(J)$  vs.  $J$  in the presence of constant noise and extracting a RB decay constant we typically find an effective increase in the error rate by a factor between 2 and 5, depending on the number of long-walk sequences employed,

and the threshold value of  $\|\vec{V}_{2D}\|^2$  used to define a long walk. Nonetheless, this approach indicates that it is possible to construct an efficient RB protocol which both increases the reported error rate, and when compared to randomly selected sequences, gives a clear, quantitative signature of model violation. Further, because calculation of  $\|\vec{V}_{2D}\|^2$  and sequence pre-selection is performed in advance, this approach alleviates the requirement to average extensively in experiment over sequences in order to reveal the skewed fidelity distribution.

#### E. GST in the presence of correlated noise

We now apply the sequence-dependent Pauli walk framework to GST in order to understand the interplay of sequence structure and temporal noise correlations in the GST estimation procedures. We begin by collating all prescribed GST sequences up to 256 gates in length (including fiducial operations and germs) [23], and calculating the corresponding walk lengths. Here we assume unit step size under application of either constant  $\hat{\sigma}_z$  or constant  $\hat{\sigma}_x$  noise process (Fig. 4a, b) such that  $\|\vec{R}\|^2 = \delta^2 \|\vec{V}\|^2$ , and plot  $\|\vec{V}_{2D}\|^2$  as a proxy for projected sequence error vs.  $J$ . We overlay the results on the calculated probability distribution of unit-step walks for RB sequences, presented as a colour scale for comparison. Points appear clumped due to the GST prescription using different fiducials (leading to different sequence lengths) surrounding a reported germ, as highlighted in Fig 4b.

Examining these data indicates that GST sequences broadly sample the range of expected fidelities in the presence of strongly correlated  $\hat{\sigma}_x$  noise, more effectively than in RB. However, their structure appears to systematically suppress measured errors in the presence of correlated  $\hat{\sigma}_z$  noise. This mimics the positively skewed of RB sequence fidelities  $\mathcal{F}$  in the presence of constant noise, as observed in the colour scale. In the presence of correlated  $\hat{\sigma}_z$  noise, only GST sequences consisting of repeated  $G_I$  germs, formally equivalent to Ramsey experiments [24], show error enhancement, limiting the utility of most germs in the protocol under this form of noise. We now explore these observations in further detail by both numerically and experimentally engineering noise of this type.

Given measured fidelities for the prescribed sequences, an open-source analysis package [25] is used to extract a large set of results characterising the performance of key gates including  $G_I \equiv \hat{I}$ , the identity,  $G_x$ , a  $\pi/2 \hat{\sigma}_x$  rotation and  $G_y$  defined similarly. One important metric calculated by the protocol is the diamond norm,  $\|G_{\text{ideal}} - G\|_{\diamond}$ , which provides a worst-case bound on the distance to the ideal gate operation. GST has found wide adoption in part because of its ability to calculate this metric which is important for formal analyses of fault-tolerance in the context of quantum error correction.

In our first test, we numerically probe the sensitivity of the GST analysis procedure to correlated noise using the aforementioned pyGSTi toolkit [25]. Starting with gates subjected to constant  $\hat{\sigma}_z$  or  $\hat{\sigma}_x$  noise, we maintain the same constant noise over all the sequences that make up the GST procedure. GST's built-in routines permit the generation of an appropriate matrix representation of all constituent operations. Because the exact mathematical representation of each gate

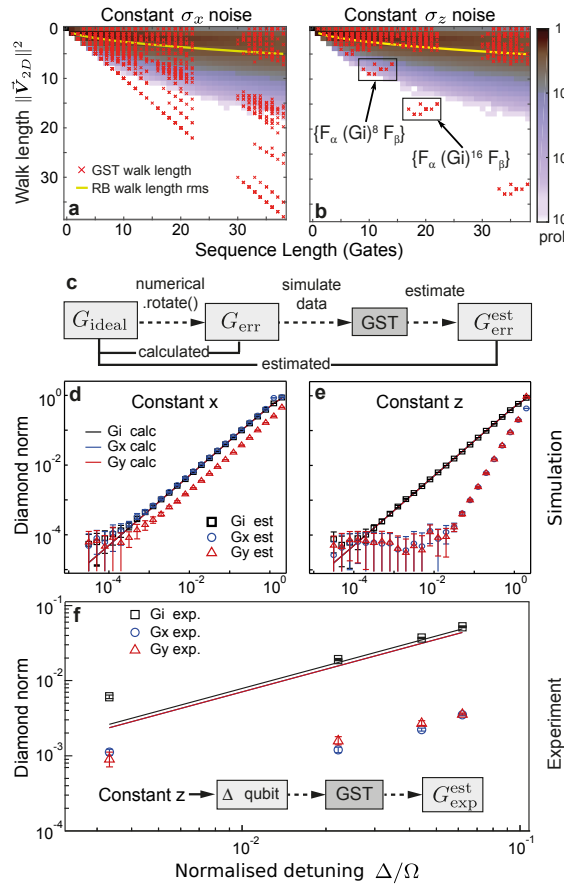


FIG. 4. **a-b)** Sensitivity of individual GST sequences to  $\hat{\sigma}_x$ ,  $\hat{\sigma}_z$  errors using the length of the sequence-dependent walk vector  $\vec{V}_{2D}$ . GST sequence walks are shown as red crosses on top of a background colour scale illustrating the distribution over  $10^6$  RB walks and their average (yellow line). In this figure we define "gates" to be constituent Clifford operations of length  $\tau_{\pi/2}$ , such that fiducial and germ operations may have different lengths in terms of "gates". **c)** Flow diagram for the numerical analysis of the diamond norm estimation under correlated errors concurrent with gates  $G$ . Deviations from the ideal case  $G_{\text{ideal}}$  are investigated entirely within the pyGSTi toolkit. **d,e)** Results of the analysis outlined above with the calculated diamond distance shown solid lines for various operations, and GST estimation results depicted as symbols. Error bars correspond to the 95% confidence interval reported by the pyGSTi routines. **f)** Experimental investigation of constant  $\hat{\sigma}_z$  errors via a deliberately engineered detuning  $\Delta$ , whose fractional value with respect to the Rabi frequency  $\Omega$  corresponds to the concurrent  $\hat{\sigma}_z$  rotation angle (see *Methods*). Markers indicate GST estimates from experimental data and solid lines represent analytical calculations from the pyGSTi toolkit.

$(G_{I,x,y})$  is known, we have two paths to evaluate gate performance (Fig. 4c). First, we may directly calculate the diamond norm ( $\|G_{\text{ideal}} - G_{\text{err}}\|_{\diamond}$ ) using the matrix representation of  $G_{\text{err}}$ . Alternatively, we may estimate it by allowing pyGSTi to simulate data using  $G_{\text{err}}$  to determine an estimated gate  $G_{\text{err}}^{\text{est}}$  via relevant fitting routines, and then extract the diamond norm ( $\|G_{\text{ideal}} - G_{\text{err}}^{\text{est}}\|_{\diamond}$ ) as would be done with real experimental

data. Comparing these two methods thus enables us to directly probe the manner in which the GST analysis package handles constant error processes.

We plot the calculated and estimated diamond norms for  $G_{I,x,y}$ , again subject to either a constant over-rotation or a constant detuning error (*i.e.* proportional to  $\hat{\sigma}_x$  or  $\hat{\sigma}_z$ , Fig. 4d-e). Here we see that while the estimated diamond norm for operators  $G_{I,x,y}$  closely match the calculated diamond norm in the presence of numerical over rotation errors, GST appears to significantly underestimate  $G_x$  and  $G_y$  errors arising from constant  $\hat{\sigma}_z$  noise, and only the diamond norm estimate for  $G_I$  appears similar to the directly calculated value. The magnitude of this discrepancy seems to increase as the size of the gate errors is reduced. The lowest attainable diamond norm is limited by the number of repetitions used in the construction of each particular data set, but is not responsible for its departure from the directly calculated value.

Experiments incorporating engineered constant  $\hat{\sigma}_z$ -noise of varying strength validate these numerical results. We generate an operation with known error magnitude and form allowing us to produce a matrix representation for the gate and hence calculate the diamond norm for the deliberately imperfect gates we apply to our trapped-ion system. Again GST produces an estimate of the diamond norm which matches the calculation for  $G_I$ ; GST yields underestimates of the diamond norm from experimental data exceeding an order of magnitude for  $G_{x,y}$  (Fig. 4f). Details of the GST data synthesis, analysis routines, and data sets employed here are presented in the Supplementary Material.

## II. Discussion

In our studies we have employed a simple analytic framework - a formalism mapping noise to error accumulation in sequences of Clifford operations - to determine the sensitivity of QCVV protocols to noise processes exhibiting varying temporal correlations. Theoretical predictions derived from this framework match experiments employing engineered noise with known characteristics, highlighting the utility of the random-walk analysis in determining sequence-dependent sensitivities of different QCVV protocols in the presence of temporally correlated noise.

We have confirmed that RB fidelity distributions over sequences are well described by a gamma distribution, even for complex noise processes inducing multi-axis errors and exhibiting gate dependence, a characteristic that has only recently been treated theoretically for QCVV protocols [21]. In addition we have demonstrated that in the presence of temporally correlated noise, the mode of the distribution over sequences is shifted towards higher fidelities than the mean and that a long tail of low-fidelity outcomes appears as suggested in [18]. Overall, the experiments reported here give clear signatures of noise processes with strong temporal correlations, which may help experimentalists seeking to interpret complex RB data sets. We believe that more detailed reporting of RB outcomes including the publication of distributions over  $\mathcal{F}$ , as well as the sequences employed, will help facilitate more meaningful comparisons between RB data sets derived from different physical systems.

Through a combination of analytical calculations, numerics, and experiments with engineered errors we have also revealed a similar bias towards high estimates of gate fidelity in GST subjected to strongly correlated  $\hat{\sigma}_z$  noise. The asymmetry we observe between the manifestation of correlated  $\hat{\sigma}_x$  and  $\hat{\sigma}_z$  noise-sensitivity has not been previously reported, to the best of our knowledge. We attribute the difference to the absence of a  $G_z$  operation. While the absence of such an operation - often enacted as a passive frame shift - appears logical, our analyses demonstrate that it has other consequences in the presence of noise with strong correlations. The observed difference in performance in the presence of correlated  $\hat{\sigma}_x$  vs.  $\hat{\sigma}_z$  noise may make GST valuable in debugging an experimental system. We note also that the evaluation of subsets of the prescribed sequences can yield highly precise calibrations without the overhead associated with the full protocol - as pointed out recently in [26].

The measured insensitivity of GST to  $\hat{\sigma}_z$  noise is concerning because a key implied benefit of GST is its ability to directly estimate the diamond norm and hence provide a rigorous upper bound on gate errors. Recent experimental work [10] on the topic claimed such upper bounds on gate errors using GST and compared these to the fault-tolerance threshold with high reported confidence and tight uncertainties. Our results reveal that, even using the developers' numerical toolkit for GST, the procedure can underestimate diamond norms for key driven operations. Furthermore, in the context of evaluating experimental data, care must be taken to suppress any form of model violations; the extracted infidelities and norms may otherwise become unreliable, which at the time of writing is not reflected in the uncertainties (*i.e.* error bars) calculated for those metrics by the toolkit.

Discussions with the authors of the GST toolkit suggest that “gauge optimisation” (effectively finding a suitable reference frame to define the qubit’s Cartesian coordinate system) may account for the discrepancies we observe between calculated and estimated diamond norms, although this phenomenology was previously only attributed to RB [27]. In our view, these observations may call into question the value of the diamond-norm metric as reported by GST when employed as an error upper-bound in the context of quantum error correction. This is because QEC will ultimately employ multiple qubits which must all be characterised in a fixed, common reference frame where independent gauge optimisation is not permitted. We therefore suggest the reporting of the worst-case estimated diamond norm encountered in the gauge optimisation procedure for a single qubit, in order to account for both model violations and the subtleties of gauge optimisation. Overall, we hope that these observations will assist in both the proper interpretation of GST data when model violation may occur, and the development of multiqubit GST frameworks that suitably set a common reference frame for all qubits.

### III. Methods

#### Experimental gate implementation

Quantum gates are implemented on a single  $^{171}\text{Yb}^+$  ion by driving its qubit transition at 12.6 GHz with microwave pulses produced by a vector signal generator (VSG, model

Keysight E8267D). The phase of the driving field is adjustable via I-Q modulation allowing us to implement rotations around any axis lying in the  $xy$ -plane of the Bloch sphere. Rotations around the  $z$ -axis are carried out as frame-updates, *i.e.* pre-calculated, instantaneous changes of the generator I-Q values. Identity operations are realised as “idle” periods, whereby no signals are applied for a time equivalent to that of a  $\pi$  or  $\pi/2$  rotation. We additionally implement pulse modulation (“RF blanking”) to suppress transients in microwave power at pulse edges. In this way, we implement the full set of Clifford gates as listed in supplementary materials.

All RB and GST sequences are uploaded to the VSG prior to the experiments and moved into volatile memory only when selected. When the number of implemented sequences is large, as is the case with GST, the latter step is the bottleneck in our experiments as sequence selection, depending on the constituent number of gates  $J$ , can take up to tens of seconds using our signal generator due to the use of the in-built, high-suppression, RF blanking which adds significant overhead.

#### Experimental noise implementation

In RB experiments correlated noise is implemented by shifting the VSG drive frequency by a fixed amount based on a list of  $N = 200$  samples from a Gaussian noise distribution (see *Supplemental Information*). The same list of noise realisations is repeated for each RB sequence in a set of given length  $J$ , yielding sets of noise-averaged fidelities. In GST experiments we implement constant noise of the same strength over all the sequences. Only four noise detunings are implemented due to the large overhead imposed by sequence selection prior to execution.

Uncorrelated noise in RB is implemented via the VSG’s external frequency modulation, whereby the frequency offset is encoded as a series of calibrated offset voltages on an arbitrary waveform generator (Keysight 33622A) and supplied time-synchronous to each gate within a sequence. Again,  $N = 200$  different realisations, each consisting of  $J$  samples are applied to each RB sequence to extract a noise-averaged fidelity. Further details can be found in the *Supplementary Material*.

#### Concurrent noise model and gate dependent errors

Deliberately induced  $\hat{\sigma}_z$  errors are implemented via a fixed detuning  $\Delta$  from the qubit’s transition frequency, which is tracked by regularly-spaced Ramsey experiments to better than 1 Hz accuracy. We apply noisy gates in which a concurrent  $\hat{\sigma}_z$  rotation modifies the unitary evolution of our physically implemented gates (only  $\hat{\sigma}_I \equiv \hat{\mathbb{I}}, \hat{\sigma}_x$  and  $\hat{\sigma}_y$ ) given by matrix-exponentiation of the corresponding Pauli-matrices  $\hat{\sigma}_{\{I,x,y\}}$  as

$$\tilde{U}(\theta, \Delta, \Omega) = \exp \left\{ -i \left[ \left( \frac{\theta}{2} \hat{\sigma}_{\{I,x,y\}} \right) + \left( \frac{|\theta| \Delta}{2} \hat{\sigma}_z \right) \right] \right\}. \quad (2)$$

The first term in the exponential corresponds to the unperturbed unitary where rotation angle  $\theta$  is chosen to be either  $\theta = \pm\pi$  or  $\theta = \pm\pi/2$ . Here the the effective error magnitude scales in relation to the Rabi frequency  $\Omega$ , and the absolute value of  $\theta$  ensures that the sign of the detuning term is pre-

served under positive and negative gate rotations.

This implementation leads to gate dependent error. Hence  $\pi$  rotations accumulate twice the phase in the presence of a nonzero  $\Delta$  as  $\pi/2$  rotations.

### Gate Set Tomography

Initial  $F_\alpha$  and final  $F_\beta$  fiducial operations are taken from the set  $\{\emptyset, G_x, G_y, G_x G_x, G_x G_x G_x, G_y G_y G_y\}$ , where  $\emptyset$  stands for no gate operation, and  $G_x$  and  $G_y$  stand for  $\pi/2$  rotations around the  $x$  and  $y$ -axes of the Bloch sphere. They are chosen to form an informationally complete set of input states and measurement bases akin to quantum process tomography. The germs used in our experiments are

$$\begin{aligned} & G_x, G_y, G_I, G_x G_y, \\ & G_x G_y G_I, G_x G_I G_y, G_x G_I G_I, G_y G_I G_I, \\ & G_x G_x G_I G_y, G_x G_y G_y G_I, \\ & G_x G_x G_y G_x G_y, \end{aligned}$$

identical to those used in reference [10]. Each of these germs is concatenated with itself up to a maximum length that successively increases as  $L = \{1, 2, 4, 8, 16, 32, 64, 128, 256\}$  and measured in all 36 combinations of the fiducials  $F_\alpha$  and  $F_\beta$ . For all 2737 sequences, we first record a baseline measurement without added error and then step through the cases of added detunings  $\Delta = \{75, 500, 1000, 1400\}$  Hz. The full data sets are passed to the pyGSTi toolkit [25] for analysis, a summary of which is provided in the *Supplementary Material*.

*Acknowledgements:* The authors acknowledge discussions with R.-Blume Kohout, P. Maunz, and E. Nielsen on GST, and R. Harper, C. Ferrie, and C. Granade for discussions on data analysis. Work partially supported by the ARC Centre of Excellence for Engineered Quantum Systems CE110001013, the Intelligence Advanced Research Projects Activity (IARPA) through the US Army Research Office, and a private grant from H. & A. Harley.

---

[1] Emerson J, Alicki R and Życzkowski K 2005 *Journal of Optics B: Quantum and Semiclassical Optics* **7** S347–S352 URL <http://iopscience.iop.org/article/10.1088/1464-4266/7/10/021>

[2] Knill E, Leibfried D, Reichle R, Britton J, Blakesstad R B, Jost J D, Langer C, Ozeri R, Seidelin S and Wineland D J 2008 *Physical Review A* **77** 012307 URL <http://link.aps.org/doi/10.1103/PhysRevA.77.012307>

[3] Wallman J, Granade C, Harper R and Flammia S T 2015 *New Journal of Physics* **17** 113020 URL <http://iopscience.iop.org/article/10.1088/1367-2630/17/11/113020>

[4] Poyatos J, Cirac J and Zoller P 1997 *Physical Review Letters* **78** 390–393 URL <http://link.aps.org/doi/10.1103/PhysRevLett.78.390>

[5] Chuang I L and Nielsen M A 1997 *Journal Of Modern Optics* **44** 2455–2467 URL <http://www.tandfonline.com/doi/abs/10.1080/09500349708231894>

[6] Holzapfel M, Baumgratz T, Cramer M and Plenio M B 2015 *Phys. Rev. A* **91**(4) 042129 URL <http://link.aps.org/doi/10.1103/PhysRevA.91.042129>

[7] Flammia S, Gross D, Liu Y K and Eisert J 2012 *New Journal of Physics* **14** 095022 URL <http://iopscience.iop.org/article/10.1088/1367-2630/14/9/095022>

[8] Granade C, Ferrie C and Flammia S T 2016 *arXiv: 1605.05039*

[9] Merkel S T, Gambetta J M, Smolin J A, Poletto S, Córcoles A D, Johnson B R, Ryan C A and Steffen M 2013 *Physical Review A* **87** 062119 URL <http://link.aps.org/doi/10.1103/PhysRevA.87.062119>

[10] Blume-Kohout R, Gamble J K, Nielsen E, Rudinger K, Mizrahi J, Fortier K and Maunz P 2017 *Nature Communications* **8** 14485 URL <http://dx.doi.org/10.1038/ncomms14485>

[11] Riebe M, Kim K, Schindler P, Monz T, Schmidt P O, Körber T K, Hänsel W, Häffner H, Roos C F and Blatt R 2006 *Phys. Rev. Lett.* **97**(22) 220407 URL <http://link.aps.org/doi/10.1103/PhysRevLett.97.220407>

[12] Rutman J 1978 *Proc. IEEE* **66** 1048–1075

[13] Hooge F N, Kleinpenning T G M and Vandamme L K J 1981 *Reports on Progress in Physics* **44** 479 URL <http://stacks.iop.org/0034-4885/44/i=5/a=001>

[14] Harlingen D J V, Plourde B L T, Robertson T L, Reichardt P A and Clarke J 2004 Decoherence in flux qubits due to  $1/f$  noise in josephson junctions *Quantum Computing and Quantum Bits in Mesoscopic Systems* ed Leggett A, Ruggiero B and Silvestini P (New York: Kluwer Academic Press) pp 171–184

[15] Fogarty M A, Veldhorst M, Harper R, Yang C H, Bartlett S D, Flammia S T and Dzurak A S 2015 *Phys. Rev. A* **92**(2) 022326 URL <http://link.aps.org/doi/10.1103/PhysRevA.92.022326>

[16] Wallman J J and Flammia S T 2014 *New Journal of Physics* **16** 103032 URL <http://stacks.iop.org/1367-2630/16/i=10/a=103032>

[17] Wallman J, Granade C, Harper R and Flammia S T 2015 *New Journal of Physics* **17** 113020 URL <http://stacks.iop.org/1367-2630/17/i=11/a=113020>

[18] Ball H, Stace T M, Flammia S T and Biercuk M J 2016 *Physical Review A* **93** 022303 URL <http://link.aps.org/doi/10.1103/PhysRevA.93.022303>

[19] Kueng R, Long D M, Doherty A C and Flammia S T 2016 *Phys. Rev. Lett.* **117**(17) 170502 URL <http://link.aps.org/doi/10.1103/PhysRevLett.117.170502>

[20] Fong B H and Merkel S T 2017 *arXiv: 1703.09747*

[21] Wallman J J 2017 *arXiv: 1703.09835*

[22] Kueng R, Long D M, Doherty A C and Flammia S T 2016 *Physical Review Letters* **117** 170502 URL <http://link.aps.org/doi/10.1103/PhysRevLett.117.170502>

[23] Blume-Kohout R, Gamble J, Nielsen E, Mizrahi J, Fortier K and Maunz P 2017 *Nature Communications* **8**

[24] Ramsey N F 1950 *Phys. Rev.* **78**(6) 695–699 URL <https://link.aps.org/doi/10.1103/PhysRev.78.695>

[25] Nielsen E, Rudinger K, Gamble J K and Blume-Kohout R 2016 pygsti: A python implementation of gate set tomography. available at <http://github.com/pygsti>

[26] Rudinger K, Kimmel S, Lobser D and Maunz P 2017 *Phys. Rev. Lett.* **118**(19) 190502 URL <https://link.aps.org/doi/10.1103/PhysRevLett.118.190502>

[27] Proctor T, Rudinger K, Young K, Sarovar M and Blume-Kohout R 2017 *arXiv: 1702.01853*